ADVANCED MATERIALS
www.advmat.de

Molecules to Masterpieces: Bridging Materials Science and the Arts

*Ferdinand F. E. Kohle, Hiroaki Sai, William R. T. Tait, Peter A. Beaucage, Ethan M. Susca, R. Paxton Thedford, and Ulrich B. Wiesner**

Art and materials innovation have always been intertwined, dating back to the earliest human creations. In modern times, however, the increasing specialization of materials science often restricts artists' access to cutting-edge materials. Here, the materials science aspects of an art-science collaboration between artist Kimsooja and the Wiesner Lab at Cornell University, are detailed. The project involves the development of a custom-made iridescent block copolymer coating by means of self-assembly, originally applied to transparent window panels of a façade for the ≈14 m tall art installation: *A Needle Woman: Galaxy Is a Memory, Earth is a Souvenir* by artist Kimsooja. After several exhibitions in the US and Europe, the installation is now part of the permanent museum collection at Yorkshire Sculpture Park in Wakefield, UK. Full characterization of the solution blade-cast coatings show shear aligned, standing up lamellar morphologies that behave as volume-phase gratings with periodicities between 300 and 400 nm. Coatings are also applied to foldable (origami) paper and converted into iridescent porous ceramic materials. It is hoped this work inspires and informs communities across materials science, the arts, and architecture.

1. Introduction

Art and materials innovation have been interconnected since the dawn of human creativity. Humans have always explored and manipulated materials to express ideas and emotions. Driven by the pursuit of novel aesthetic properties and innovative ways to exploit those, artists acted as early material innovators. For example, prehistoric artists composed finger paint from natural materials to create vivid cave art.[1] They used rust powder (Fe_2O_3, yellow to deep red) and charcoal (black) as pigments, aluminosilicate clays to adjust the paint's texture, and organic binders like marrow, fat, urine, saliva, or blood to hold the paint together.[2] Despite lacking a deeper understanding of the underlying material structure–property relationships (i.e., of organic-inorganic hybrid composite paints), trial-and-error material exploration guided by observation and experience led to remarkable material achievements within the arts. Throughout history, the relationship of artistic and material innovations is evident: Roman dichroic glass (4th century), such as that composing the Lycurgus Cup, used Au/Ag alloy nanocrystals for color and light mastery;[3] Chinese porcelain (6th century onward) blended kaolin clay with minerals for an elegant translucent finish;[4] Islamic Lusterware (8–14th centuries) achieved a metallic sheen through a two-step firing method;[5] Gothic stained glass (11–15th centuries) infused glass with metallic salts for vivid hues that painted light into architecture[6]; and Renaissance oil paintings (15th century) mixed linseed oil with pigments allowing artists unprecedented flexibility to explore depth and subtlety, and opening new vistas of realism in their work.[7]

With the emergence of scientific disciplines in the 16th and 17th centuries,[8] the exploration and manipulation of materials gradually transitioned into the domain of scientific research, creating barriers[9] for artists who wish to use state-of-the-art materials in their work. This shift has left artists dependent on novel materials being made available as commercial products, a translation that not all materials will undergo. Despite these barriers, many artists are driven to explore state-of-the-art materials and processing methods for their unique properties and aesthetics, and the potential to express contemporary themes. One of the best ways artists can gain access to cutting edge materials is interdisciplinary collaborations between artists and scientists

---

F. F. E. Kohle, H. Sai, W. R. T. Tait, P. A. Beaucage, E. M. Susca,
R. P. Thedford, U. B. Wiesner
Materials Science and Engineering
Cornell University
Ithaca, NY 14853, USA
E-mail: ubw1@cornell.edu
F. F. E. Kohle
Chemistry and Chemical Biology
Cornell University
Ithaca, NY 14853, USA
H. Sai
Center for Regenerative Nanomedicine
Northwestern University
Chicago, IL 60611, USA
W. R. T. Tait, R. P. Thedford
Robert Frederick Smith School of Chemical and Biomolecular Engineering
Cornell University
Ithaca, NY 14853, USA
P. A. Beaucage
NIST Center for Neutron Research
National Institute of Standards and Technology
Gaithersburg, MD 20899, US
U. B. Wiesner
Design Tech
Cornell University
Ithaca, NY 14853, USA

The ORCID identification number(s) for the author(s) of this article can be found under https://doi.org/10.1002/adma.202413939

DOI: 10.1002/adma.202413939

(art-science collaborations). Such partnerships are not without their own challenges[9] but often result in groundbreaking artworks. Notable examples include "Alba" (2000), a genetically modified, luminescent albino rabbit created by artist Eduardo Kac and biologist Louis-Marie Houdebine at the French National Institute of Agronomic Research. Alba who glows green under black light,[10] became a symbol for the possibilities of bioengineering as well as a point of controversy over animal rights. Similarly, "The Nano Sculptures" (2014), a pioneering project by artist Jonty Hurwitz and researchers at the Karlsruhe Institute of Technology (KIT), involved creating microscopic silicon sculptures using multiphoton lithography, pushing the boundaries of scale and perception in sculpture.[11] Frederik De Wilde's "NanoBlck-Sqr #1" (2014), developed with Rice University, features a square meter canvas of black carbon nanotubes that absorb an exceptionally high percentage of visible light redefining the visual and conceptual limits of blackness in art.[12] A race to the "blackest" artwork that was later continued by Anish Kapoor using VANTAblack, a material by Surrey NanoSystems that is composed of vertically aligned carbon nanotube arrays absorbing up to 99.965% of visible light.[13]

Color, with its unparalleled ability to captivate both artists and audiences, is a fundamental element in the artistic manipulation of materials. The perceived color of an artwork is dependent on the viewer, the light source and the physical and chemical properties of the art materials used. On an objective level (excluding the viewer) color stems from the interaction of light waves with electrons through distinct chemical and physical mechanisms.[14] Knowingly or unknowingly, artists have harnessed nearly all these origins of color to enrich their creative expressions. Perhaps the most mesmerizing color phenomena, however, is structural color. It holds a special allure due to its bright, highly saturated colors and the dynamic visual experiences it can create. Unlike pigment-based color, structural color arises from scattering, diffraction, and interference effects of light interacting with micro- and nanostructured materials with critical dimensions on the scale of the wavelength of visible light (λ_{vis} between 400 and 800 nm).[15] This interaction can result in iridescence, where colors shift and change based on the angle of light and the viewer's perspective, offering a level of visual complexity and vibrancy difficult to achieve through other means.

Structural color is naturally found in opals, nacre (mother of pearl), butterfly wings, bird feathers, and beetle exoskeletons which historically have been sources of decorative materials.[16] Unlike pigments, such examples are resistant to photobleaching, making it an environmentally friendly alternative as a coloring method. However, replicating the complexity and durability of naturally occurring structural color in synthetic materials, especially scaling to large areas, has proven challenging. The fabrication of these materials requires precise control over material architectures on the nanoscale, which can be difficult and costly.[15] Moreover, ensuring that these colors remain stable under various environmental conditions further adds to the challenge of creating synthetic structural colors that are as vivid and enduring as those found in nature. Methods to synthetically impose nanostructure on a material include top-down approaches, such as nanolithography and controlled laser etching, and bottom-up approaches, such as electrochemical deposition and self-assembly enabled methods, e.g., hard templating, soft templating, and co-assembly.[17–21] Top–down methods tend to require expensive equipment and complex processing limiting scalability across large areas, while bottom-up methods tend to have defects typical in soft matter approaches. Self-assembling materials, i.e., materials that regularly order themselves to reach a thermodynamic equilibrium, however, do have the appeal of often being solution processible, and therefore scalable and amenable to techniques such as roll-to-roll processing.

Synthetic materials displaying structural color, including colloidal photonic crystals, dielectric metasurfaces demonstrating resonance and, or scattering, and metallic assemblies with plasmonic properties, have found numerous small- and medium-scale applications, such as in optical devices, displays, sensors, optical memory storage, anti-counterfeiting measures, photocatalysis, waveguides, radiative cooling, and solar cells.[15,22–27] These materials are also being utilized for sustainability purposes, including bleach-resistant, ultra-light, and, in some cases, dynamically tunable pigment replacements[23,28,29] and colored 3D printing filaments,[30,31] as well as for decorative applications in car paint,[25] textiles, fashion garments,[16] and design objects. Despite significant progress in creating nanostructured materials, large-scale architectural applications remain rare. Most architectural-scale uses are limited to research on radiative cooling,[32] and decorative applications that utilize multilayer films or self-assembling colloidal particles amenable to coating techniques.[15,23] Such materials often portray a synthetic and controlled look, lacking the organic randomness of natural iridescence, which is visually more complex and often exhibits subtler effects with a sense of depth and texture, adding to the richness of the visual effects.

Block copolymers (BCPs) present one of few viable building blocks for the bottom-up self-assembly of complex nanostructures of various length scales in a manner that is both scalable and cost-efficient.[33] This efficacy stems from the ability to tune their molecular composition and their inherent capability to self-organize into complex nanoscale architectures. Furthermore, by realizing dimensions of such nanostructures on the order of the wavelengths of visible light, it is feasible to create photonic materials that reflect vibrant, iridescent colors, thereby conceptually mimicking the molecular self-organization observed in living organisms displaying structural color.[34]

Numerous photonic architectures have been self-assembled from BCPs, spanning from structures with long-range order, such as closely packed micelles,[35] hexagonally packed cylinders,[36] double diamonds,[37] gyroids,[38] and cubic and correlated networks,[39] to systems exhibiting only short-range order like photonic glasses.[40] However, research over the past twenty years has predominantly concentrated on developing lamellar structures using linear and brush block copolymers.[41] Photonic materials other than films, such as gels, have also been demonstrated using BCP architectures swelled up by solvents.[42] Moreover, due to the ability of amphiphilic BCPs to selectively compatibilize individual blocks with additives, photonic crystals using BCP-inorganic nanoparticle hybrids and photonically active, BCP-directed hybrid resin materials have been described.[43,44] However, combining self-assembly processes with traditional painting or coating practices in such a way that materials can be applied to a surface resulting in structural coloration remains practically challenging, as artificial self-assembling materials usually lack pathway selectivity. Current approaches typically involve slow solvent evaporation or thermal annealing steps, allowing materials to reach thermodynamic equilibrium structures, that are not readily applicable to industrial processes.

Furthermore, connecting advanced materials with the arts at the human-to-architectural scales is a major challenge. Exploratory materials first fabricated in research laboratories are typically produced at the sub-gram to gram levels incompatible with the large material amounts required, e.g., in architecture. Similarly, novel materials and processing methods often take years before being translated from research to large scale commercial production.[45] These are well-known obstacles that limit the use of state-of-the-art materials out of research laboratories (e.g., BCPs as color agents) for ambitious applications in the fields associated with arts and architecture.

Here, we present an unusual project that bridges the realms of materials science, the arts, and architecture in a unique and groundbreaking manner. In the following, we describe the development of a BCP-based iridescent window coating which was created specifically for its use as an architectural façade for the 46-foot-tall, 4.5-foot-wide art installation titled "*A Needle Woman: Galaxy Was a Memory, Earth is a Souvenir*" (2014) by renowned Korean-American artist, Kimsooja, architect, Jaeho Chong, and first exhibited at Cornell under the auspices of the Cornell Council for the Arts (CCA) led by Stephanie Owens (**Figure 1**; Figure S1, Supporting Information).[46] The inspiration for this project was sparked during an initial conversation between the artist and the scientists, where an iridescent polymer sample – originally created for a different purpose – was presented (Figure S1, Supporting Information). The striking optical properties of the material, emerging from the self-organizing of polymeric molecules, captivated the team and led them to explore the development of a vivid structural color façade for an installation. Thereby, the project aimed to parallel the natural processes of molecular self-assembly and structural color, like those seen in the morpho butterfly (Figure S2, Supporting Information), and Kimsooja's use of fabric to weave layers of meaning, both revealing how simple elements (threads and molecules) can form complex structures that uncover hidden meanings and evoke shifts in perception.

To realize this objective, the team engineered a linear block copolymer, poly(styrene-*block*-*tert*-butyl methacrylate) (StB), with an exceptionally high molecular mass. Through a phase of material exploration driven by both scientific insight and aesthetic vision (Figure S2, Supporting Information), the team developed a manual blade-casting technique of a StB solution. This method resulted in the formation of iridescent films through BCP self-assembly during solvent evaporation. To the authors' knowledge, this endeavor represents the first aesthetic application of linear BCPs on an architectural scale. After its European debut at FRIEZE Sculpture in London in 2018, the installation has now entered the permanent collection at the Yorkshire Sculpture Park, a museum in Wakefield, UK, where it continues to captivate and engage a large number of annual park visitors, e.g., close to 400 000 in 2022 alone.[47] From its creation and debut in 2014 through today, the installation's striking block copolymer-based structural color has not degraded, despite long tenures outside in sunlight and facing the variation of light and temperature exposure that comes with the changing seasons.

In the following, in three stages we present the rationale and process starting at the molecular design of the BCP to the final application as a window panel. Stage one focuses on polymer solution properties, nanostructure formation via bottom-up self-assembly and shear-alignment of the lamellar architecture, the interrelationship of molar mass and domain spacing, and resulting optical properties. Stage two describes the challenge of scaling the process from the lab bench, i.e., working with milligrams, milliliters, and square centimeters, to achieving architectural scale outcomes, i.e., working with grams, liters, and square meters, in particular addressing polymer synthesis and BCP film formation challenges. Stage three introduces the final window panel design that was used for the installation.

The paradigm of using ultralarge, linear BCPs as sources for structurally colored media is further explored in both canvas and material palette, where StB is demonstrated on a paper substrate, and a second set of large BCPs, poly(styrene-*block*-2-dimethylaminoethyl methacrylate) (SA), is co-assembled with a polysilazane ceramic precursor and processed into, to the authors' knowledge, the first example of a BCP-self-assembly directed porous and structurally colored ceramic.

By transitioning BCP self-assembly materials from the domain of scientific research to their use as contemporary art materials through an art-science collaboration, we celebrate and hope to reinvigorate the longstanding relationship between material innovation and the arts.

2. Experimental Section

2.1. Materials

For the sequential living anionic polymerization of AB diblock copolymers (StB and SA, *n*-butyllithium (1.6 M in hexanes, Acros Organics), *sec*-butyllithium (1.4 M in hexanes, Sigma-Aldrich), dibutylmagnesium (1.0 M in heptane, Sigma–Aldrich), diisobutylaluminum hydride (1.0 M in hexanes, Sigma–Aldrich), triethylaluminum (1.0 M in hexanes, Sigma–Aldrich), trioctylaluminum (25 wt.% in hexanes, Aldrich), methanol (anhydrous, J. T. Baker), and toluene (HPLC grade, J. T. Baker) were used as received. 1,1-diphenylethylene (DPE, >99%, TCI America) was vacuum distilled and stored under inert atmosphere at −40 °C. Cyclohexane (99.5%, Sigma–Aldrich) was dried using n-butyllithium with 1,1-diphenylethylene as an indicator and was vacuum distilled into the reaction flask prior to use. Tetrahydrofuran (THF, HPLC grade without inhibitor, J. T. Baker) was used immediately after opening the bottle, dried using n-butyllithium with 1,1-diphenylethylene as an indicator, and vacuum-distilled immediately prior to usage. Styrene (99%, Sigma–Aldrich) was stirred for an hour in an inert environment with dibutylmagnesium powder, dried from its heptane solution, and was subsequently vacuum distilled into a frozen ampoule that was kept at liquid nitrogen temperature until usage. *Tert*-butyl methacrylate (tBMA) (>98%, TCI America) was freeze-pump-thawed three times, titrated with a 1:1 volume-to-volume (v/v) mixture of diisobutylaluminum

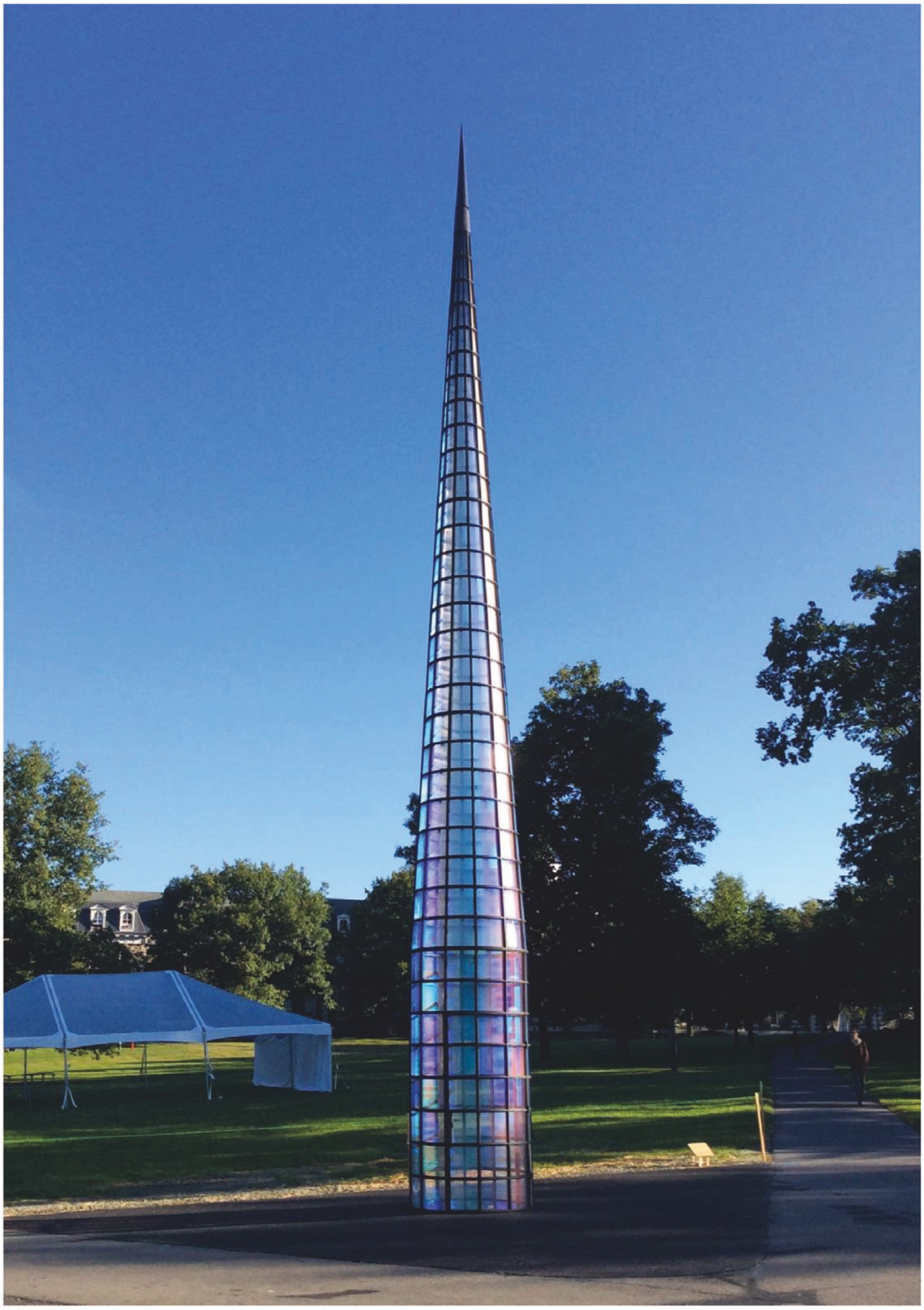

Figure 1. *A Needle Woman: Galaxy Was a Memory, Earth is a Souvenir* (Kimsooja). Cornell Arts Quad. Steel installation (1.3 m diameter at base, ≈14 m height), window panels coated with iridescent self-assembled lamellar block copolymer film whose lamellar sheets were oriented vertically along the tower long axis. Today, this structure is part of the permanent museum collection at Yorkshire Sculpture Park in Wakefield, UK.

hydride and triethylaluminum solutions under inert atmosphere at ≈0 °C until a yellow color persisted, and stirred for an hour before being vacuum distilled into a frozen ampoule immediately prior to usage. Monomer 2-(dimethylamino)ethyl methacrylate (DMAEMA) (99%, stabilized, Acros Organics) was purified over a 1:1 (v/v) mixture of triethylaluminum and trioctylaluminum, freeze-pump-thawed three times, and left stirring for >1 h after the third thaw until the solution had a persistent color; the DMAMEA was then distilled into a frozen ampoule immediately prior to usage.

For light scattering and film casting, decahydronaphthalene (mix of cis and trans, anhydrous 99%, Sigma–Aldrich), THF (anhydrous, Sigma–Aldrich), benzyl acetate (99%, Alfa Aesar), allyl acetate (99%, Sigma–Aldrich), and toluene (anhydrous, Sigma–Aldrich) were used as received. For hybrid film materials, Durazane 1800 (Merck EMD Electronics) and

(3-glycidyloxypropyl)trimethoxysilane (GLYMO) (98%, Sigma–Aldrich) were used as received.

2.2. Synthesis of Block Copolymers

2.2.1. StB

A standard Schlenk line with argon as inert gas and a glovebox with nitrogen environment were used in the anionic polymerization of StB. Due to the high viscosity of the reaction mixture, a high-power magnetic stirrer and a samarium cobalt magnetic stir bar were used for mixing. For a targeted StB molar mass of 1500 kg mol^{-1}, ≈1 L of THF was vacuum distilled into a 2 L one-neck reaction flask equipped with a Rotaflo valve. To this flask, ≈40 mL of freshly prepared styrene and 0.475 mL of *sec*-butyllithium solution (0.07 M, diluted from 1.4 M with cyclohexane) were added sequentially, and the polymerization was carried out at −78 °C for 1 h. Within a minute, the orange reaction mixture became viscous. After an hour, distilled DPE was diluted ten times with distilled THF inside a glovebox, titrated with a 0.07 M *sec*-butyllithium solution until a slight pink color persisted, and 0.15 mL of this pink solution was transferred to the reactor with a needle and a syringe. The solution turned red in color upon addition of DPE. Then, 40 mL of distilled tBMA was added to the reactor, and the polymerization proceeded at −40 °C for ≈2h. The solution turned opalescent after ≈10 min. Finally, the polymer was terminated with methanol, and precipitated in a 2:1 methanol/deionized water mixture and dried with a diaphragm pump for 12–24 h. It was then further dried in a vacuum oven first at 50 °C for 24 h and finally at 80 °C for another 24 h.

2.2.2. SA

The SA diblock copolymer was also synthesized via sequential anionic polymerization, using a method adapted from a procedure described elsewhere.[48] Approximately 1 L of THF was first purified using n-butyllithium, with DPE as a colorimetric indicator, and distilled through a Schlenk line into a 2 L reactor. The reactor was transferred into a nitrogen glovebox, where a small amount of DPE was added, followed by dropwise addition of *sec*-butyllithium, until the solution turned a very light pink, confirming the purity of the solvent. The THF was left at room temperature for 3−4 h to let any remaining living *sec*-butyllithium degrade. The reactor was then brought out of the glovebox, chilled to −78 °C, and had nitrogen actively purging through its volume. Diluted *sec*-butyllithium was added to the reactor. Distilled styrene was then added via cannula transfer. The styrene was allowed to react for ≈1 h at −78 °C, and the resulting polymer then capped with DPE diluted ten times with distilled cyclohexane. Distilled DMAEMA was added to the reactor dropwise through cannula transfer. The DMAEMA was allowed to react at a temperature maintained ≈−50 °C for 1 h, and then was quenched with degassed methanol. The polymer solution was concentrated using a rotary evaporator. The viscous solution was then precipitated into stirring methanol. The precipitated polymer was collected via vacuum filtration and then dried in a vacuum oven overnight at 40 °C with a dish of phosphorus pentoxide in the oven as an additional drying agent.

2.3. Polymer Characterization

Molar fractions of polystyrene (PS), poly(*tert*-butyl methacrylate) (PtBMA), and poly(2-dimethylaminoethyl methacrylate) (PDMAEMA) blocks were determined via proton nuclear magnetic resonance (^{1}H NMR) using a Varian INOVA-400 spectrometer. For example, for StB, spectra were integrated in two regions: between 6.2 and 7.2 ppm (corresponding to the 5 aromatic protons of the polystyrene block) and between 0.8 and 2.4 ppm (corresponding to the remaining 3 polystyrene backbone protons and all 14 protons of the poly-*t*-butylmethacrylate block). These integrals were used to calculate the block fractions given in **Table 1**. For the SA diblock copolymer, proton NMR was run on a Bruker AV500 spectrometer. These spectra were integrated between 6.2 and 7.2 ppm for the polystyrene block, and between 4.0 and 4.2 ppm for the 2 protons on the carbon in the dimethylaminoethyl group adjacent to the ester oxygen. These integrals were used to calculate the block fractions.

Polymers were characterized by gel permeation chromatography (GPC) equipped with a Waters 410 refractive index detector, using THF as the eluent. However, due to the high molar mass of polymers, elugrams could not be quantitatively analyzed against a polystyrene standard curve. Instead, the molar mass of the different StB and SA batches were determined by light scattering measurements in THF to create Zimm plots using a Brookhaven BI-200SM Static Light Scattering System, equipped with a 632.8 nm He:Ne laser and an avalanche photodiode detector. Molar mass was determined by double extrapolation to zero concentration and zero angle from a series of measurements at different polymer concentrations and at different scattering angles.[49] Steady shear rheological measurements of StB toluene solutions, 7.5 and 10 weight percentage (wt%), were carried out at room temperature on an ARES–LS rheometer (Rheometric Scientific) equipped with a cone and plate fixture of diameter 10 mm and cone angle 1°. Measurements spanned shear rates, $\dot{\gamma}$, from 0.1 to 1000 s^{-1}. To reduce solvent evaporation, a dome of aluminum was placed around the sample during measurements.

2.4. Film Formation and Characterization

StB BCP films were manually blade-cast using glass coverslip substrates (Fisher Scientific) and Scotch tape (3M) as spacers as described in the main text. Typical casting conditions included 3–5 layers of scotch tape (≈50 µm gate height per layer), casting speeds of 0.5–1 cm s^{-1}, and StB solution concentration of 10 wt%. Gate height and film thickness were measured using a micrometer screw gauge. At least ten measurements were taken at different film locations and results averaged.

The domain spacing of cast films was determined by ultra-small-angle X-ray scattering (USAXS) measurements performed at beamline 9-ID-C of the Advanced Photon Source[50,51] operating at 17.6 keV. Data were reduced using the Indra package

Table 1. Polymer characterization results for StB from Zimm plots, ^{1}H NMR, USAXS, and optical transmission diffraction measurements for different batches of StB-1 to –4 diblock copolymer solutions and films derived from blade-casting. Columns display, from left to right, weight average molar mass, M_w, radius of gyration, R_g, second virial coefficient, A_2, mole fractions of PS and PtBMA, domain spacing, d, as determined by USAXS, and grating periodicity, Λ_g, from optical transmission diffraction measurements.

Sample	M_W [kg mol^{-1}]	R_g [nm]	A_2 [x10^{-4} cm^3 mol g^{-2}]	PS:PtBMA [%:%]	d (*USAXS*) [nm]	Λ_g (*Diff.*) [nm]
StB-1	1255 ± 18	64.2 ± 2.1	3.591 ± 0.092	36.8:63.2	255	258 ± 2
StB-2	1412 ± 51	66.5 ± 1.2	3.860 ± 0.063	39.2:60.8	282	282 ± 2
StB-3	1623 ± 28	69.8 ± 2.9	3.586 ± 0.052	38.5:61.5	304	303 ± 1
StB-4	2601 ± 19	91.1 ± 0.6	3.725 ± 0.081	29.9:70.1	355	343 ± 2

and desmeared. Samples were prepared as stacks of up to 20 thin films prepared with the same orientation and secured with Scotch tape (3M) to increase signal intensity. The scattering background contribution from the two layers of tape measured separately was subtracted from all final patterns.

Transmission electron microscopy (TEM) images were acquired on a FEI Tecnai T12 microscope operated at accelerating voltage of 120 kV in bright-field mode equipped with a high-resolution, thermoelectrically cooled Gatan Orius dual-scan CCD camera. StB samples were cast on a poly(ethylene terephthalate) (PET) substrate (thickness 120 ± 3 µm, PET UV-laminate, provided by Laumont Photography) and prepared for TEM analysis by cryo-sectioning using a Leica EM UC7 cryo-ultramicrotome with stage and blade set to –65 °C. Films were mounted on holder stubs using OCT compound (Tissue-Tek) in orientations such that the cross-sections would be either parallel or perpendicular to the casting direction. A wet cryo 35° diamond knife (DiATOME) was used to cut StB films with target thickness of 65 nm into a 60:40 (v/v) dimethyl sulfoxide:water bath. Floating sections were then transferred to copper TEM grids using a Deluxe Perfect Loop (Electron Microscopy Sciences). No further sample preparation was necessary as the relative atomic mass contrast between the two blocks was sufficient to distinguish them in TEM even without contrast enhancing film staining procedures.

Scanning electron microscopy (SEM) images were acquired using a TESCAN MIRA3 LM FE-SEM operated at an accelerating voltage of 5 kV. StB films cast on paper were prepared for SEM by sputter coating with Pd/Au for 20 s at 30–40 mA. Conductive copper tape was applied postsputtering to ensure samples had electrical grounding to the sample stub.

2.5. Optical Measurements

Angular dependent transmission and reflection spectra of StB films were measured using a homebuilt tunable spectroscopy setup. The setup consisted of a collimated and polarized tungsten light source for illumination (spot size of ≈0.5 cm) and a fiber-optic Ocean Optics QE65000 spectrometer for detection. The sample was mounted on the rotational axis of a goniometer holding the detection fiber and a lens to focus the signal into the fiber. The angle of incidence (α) and the detector angle (β) could be set independently. Samples were cast on a poly(methyl methacrylate) (PMMA) substrate (thickness 1 mm). All spectra were corrected for the spectral profile of the tungsten light source.

2.6. Window Panel Fabrication

Window panels were fabricated using a self-developed casting-lamination process. To achieve homogenous color throughout the tower, at least four different synthesis batches with different molar mass were mixed and dissolved in toluene to a 6.5–7.5 wt% casting solution. Films were manually bar-cast on a PET lamination sheet (thickness with adhesive layer of 120 ± 3 µm, 16″ x 16″ PET UV-laminate, provided by Laumont Photography) using an anodized alumina bar with 5–6 layers of scotch tape (3M) as spacers, and at shear rates between 80 and 140 s^{-1}. The PET sheet was adhered to a flat steel plate by using a water-soap mixture (99:1 volume fraction). The films were left to dry in a fume hood. The dried films were laminated across the StB coated laminate film with a second layer of PET for protection by Laumont Mounting and Framing, Queens, NY. The sandwich was then cut to the respective size of the previously heat bent PMMA plates and manually laminated to the concave surface.

2.7. Preparation of Hybrid Films/Ceramics

The SA was dissolved in 0.5:0.35:0.15 toluene: allyl acetate: benzyl acetate (ratio by weight) ternary solvent at a concentration of 12.5 wt%. For the “dark version” (more structural color in reflection, less in transmission) of the materials, 0.1 wt% carbon black was added to the ternary solvent before dissolution of the polymer. The solution was stirred until a homogenous, viscous dope was achieved; this usually took >6 h. Durazane 1800 was then added to the viscous solution to achieve a 1.37:1 Durazane 1800: polymer weight ratio. In samples that also had silicate precursors in addition to the Durazane 1800, unhydrolyzed GLYMO was added in a 0.13:1 GLYMO: polymer weight ratio; this resulted in a 1.5:1 inorganic precursor: polymer weight ratio for these samples. The dope was stirred at least an additional 2 h; longer stir times (>12 h) would result in colors more into the yellows/oranges, while shorter times resulted in majority coloration of blues/greens (assuming angle of incidence/viewing = 0). On a glass substrate, a gate height of 9 strips of 3M magic tape (570 µm thickness) was set. A line of the polymer solution dope was cast between the gates, and a film was generated by doctor-blading the solution down the substrate with a bar at the gate height; the bar was moved at ≈0.5 cm s^{-1}. Faster blade speeds would result in a more transparent film. The resultant film was left to dry in the hood for >12 h, and subsequently heated to 130 °C for 12 h, resulting the hybrid films. Hybrid films were then put in a ceramic

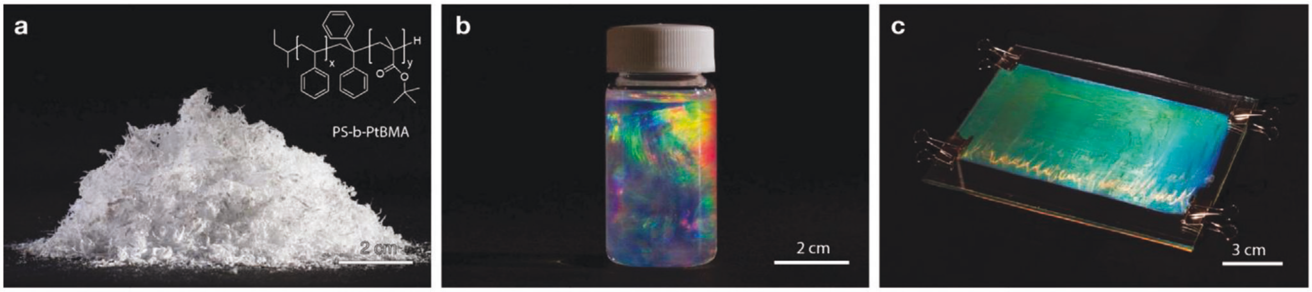

Figure 2. Different states of the block copolymerStB. a) Photograph of ≈10 g dry StB after synthesis; Inset: Chemical structure of StB. b) StB in toluene solution in a 20 mL glass vial. Incident light from the right. c) A dry film of StB sandwiched between a glass substrate and a cover glass.

boat for thermal processing. The hybrid films were then heated to 1000 °C (ramp rate 1.5 °C min^{-1}) under ammonia for 3 h to generate the final iridescent ceramic materials.

3. Results and Discussion

Photonic crystals are an example of synthetic materials that contain periodic structures and exhibit structural color. These materials are typically used in optoelectronic devices and fabricated by expensive top-down approaches, such as electron-beam lithography and etching methods. Alternatively, photonic structures can be created from BCPs that spontaneously self-assemble into periodically ordered structures, thereby mimicking the bottom-up fabrication process often found in nature. In an AB diblock copolymer two polymeric chains (blocks), each made from a different kind of polymer and denoted as block A and B (**Figure 2**a), are covalently linked together. Morphology and structural dimensions (domain spacing, *d*) are determined by the relative volume fractions of the blocks, block chemistry, their tendency for microphase segregation (described by the Flory–Huggins interaction parameter, χ), and overall molar mass of the BCP.[52]

With increasing relative volume fraction of block A different morphologies are accessible, including spherical (S), cylindrical (C), gyroidal (G), or lamellar (L) structures and their inverse (Figure S3, Supporting Information). For lamellar structures, the periodic spacing between the two blocks is described by the domain spacing, *d*, and depends on BCP molar mass. If BCP molar mass and resulting *d* are not sufficiently large, visible light cannot efficiently couple to the lamellar structure and no iridescent color is observed.

In this project we used the AB diblock copolymer StB (Figure 2a). The choice of this particular BCP was based on a number of design requirements for the final installation, including the need to produce of order a kilogram of polymer with a relatively narrow molar mass distribution, solution processability in painting-compatible solvents, as well as chemical and structural stability under outdoor conditions including temperatures between −20 and 50 °C and exposure to rain and sunlight. PS and PtBMA blocks have a Flory–Huggins interaction parameter of 0.08–0.10,[53] making it straightforward to select a single solvent that can dissolve both blocks even at ultrahigh molar mass required for solution processing. Both PS and PtBMA blocks have glass transition temperatures above 100 °C, making them mechanically stable in the expected outdoor temperature range.

StB was synthesized via sequential anionic polymerization (see Experimental Section and Figure S4, Supporting Information). Four different batches of StB (StB-1 to StB-4) were synthesized with varying molar mass. We targeted a 50:50 volume fraction of PS:PtBMA to achieve a lamellar morphology and molar mass between 1500 and 2000 kg mol^{-1}. BCP composition (% PS:% PtBMA mole fraction) and molar mass were determined from a combination of proton nuclear magnetic resonance spectroscopy (^{1}H NMR) and Zimm plot analysis of light scattering data (Table 1; Figures S4–S6, Supporting Information). Molar mass ranged from ≈1250 to 1600 kg mol^{-1} for StB-1 to StB-3 and reached ≈2600 kg mol^{-1} for StB-4 (Table 1). All batches contained significant amounts of PS homopolymer as indicated by a second peak at longer elution times in the GPC measurements, indicating that despite our best efforts to exclude water and/or air from the living anionic polymerization process, some of the organolithium chain ends were prematurely terminated in the process of DPE end capping and second monomer addition (Figure S6, Supporting Information). The total amount of initiator used for a 50 g synthesis of 2000 kg mol^{-1} BCP is only 25 µmol, emphasizing the difficulty to achieve the high degree of air and water exclusion necessary for successful block copolymer synthesis. The large molar mass of sample StB-4 can be attributed to a larger number of PS homopolymer chains terminated after polymerization of the first block (see GPC elugram in Figure S6, Supporting Information), followed by polymerization of the second block from fewer remaining chains that continued until all tBMA monomer was depleted, leading to a large second block for the living chains and a PtBMA mole fraction of over 70% (see Table 1).

Photographs in Figures 1 and 2a–c (also see **Figure 3**f) summarize the different states of BCP StB throughout the project. Figure 2a shows a photograph of the diblock copolymer StB after synthesis and precipitation in a methanol/water mixture and subsequent drying. Under these conditions the resulting BCP appears as a white powder, with white light randomly scattered off the material in all directions. Figure 2b shows a photograph of StB in a toluene solution with white light illumination from the right. Here, different color domains are visible spanning the entire visible spectrum, i.e., from blue to red, suggesting different orientations of a lyotropic liquid crystal solution. Figure 2c shows a photograph of a StB polymer film cast from a solution comparable to the one in Figure 2b. The final installation in Figure 1 exhibits BCP StB cast into a thin film on transparent panel substrates resulting in strong iridescent colors. Unlike the dry powder state depicted in Figure 2a, during the solvent

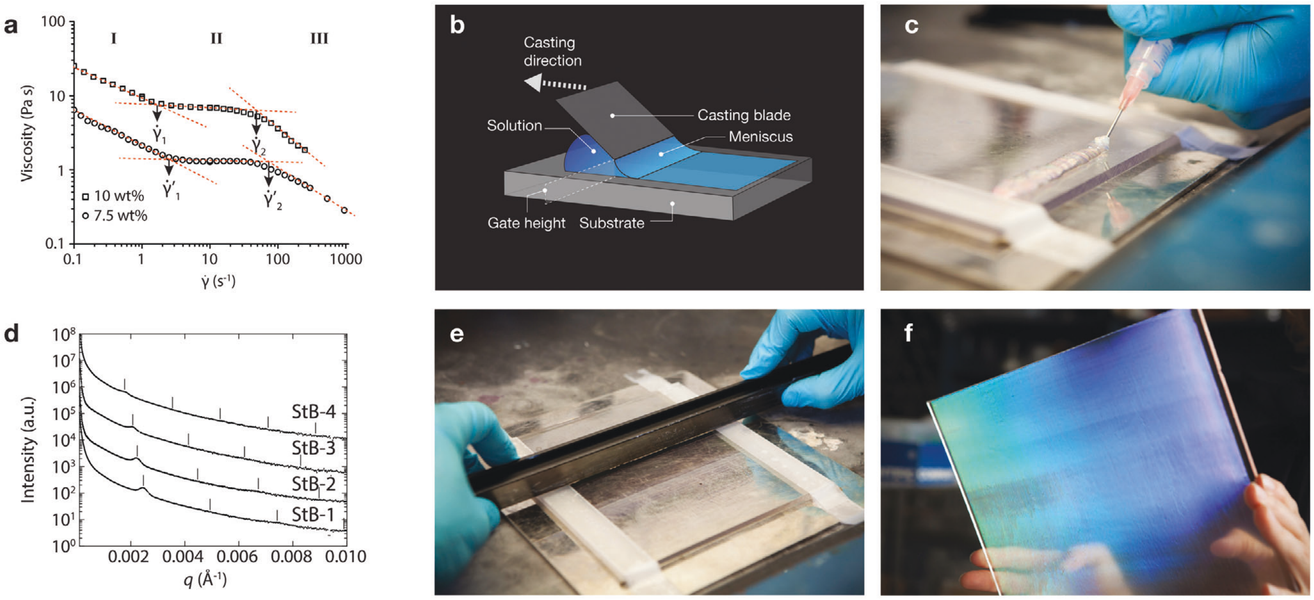

Figure 3. Details of the solution blade-casting process. a) Viscosity versus shear rate for two different StB solutions (10 wt% vs 7.5 wt%) indicating critical shear rates, $\dot{\gamma}$. b) Schematic illustration of solution blade-casting process. c) Photograph illustrating casting the polymer dope. d) Results of USAXS measurements on StB films from batches with different molar mass. e) Photograph illustrating solution blade-casting process. f) Photograph of a cast prototype StB film on a flat PMMA substrate.

evaporation step of the thin BCP film formation, StB chains undergo spontaneous microphase separation into a nanoscale morphology, whose length scale, periodicity, and orientation give rise to iridescent colors.

Whether a uniformly colored and transparent StB film can be cast from a solution depends on a number of parameters, including the solvent used, the StB solution concentration, and the shear rate during casting. For example, THF as a solvent dissolved BCP StB but prohibited appropriate structure formation, likely due to its propensity to preferentially dissolve PS and to its fast evaporation rate that leads to water droplet condensation. In contrast, toluene, chloroform, and xylenes lead to uniform shear-cast films. Toluene was selected as the processing solvent of choice due to its relatively slow evaporation time and low toxicity.

To gain insights into the properties of StB solutions in toluene we performed steady shear rheological measurements with a 10 wt% solution of the batch StB-2. Solution viscosity was measured performing a shear rate sweep. The double logarithmic plot in Figure 3a shows three distinct regimes (I, II, III). Regime I and III are characterized by shear thinning, whereas regime II shows a pseudo-Newtonian behavior where viscosity is independent of shear rate between $\dot{\gamma}_1 \approx 2$ s^{-1} to $\dot{\gamma}_1 \approx 50$ s^{-1}. This plateau is shifted toward larger shear rates for a more dilute solution of 7.5 wt% (about $\dot{\gamma}'_1 \approx 3$ s^{-1} and $\dot{\gamma}'_2 \approx 80$ s^{-1}). Similar melt rheological behavior of lamellae-forming diblock copolymers has been described under large amplitude oscillatory shear, in which three frequency regimes of orientation were elucidated via ex-situ X-ray scattering experiments of sheared samples.[54] While in the low and high frequency regimes the lamellar morphology oriented parallel to the substrate, in the intermediate frequency regime lamellar sheets oriented along the shear direction perpendicular to the substrate. We postulated from our viscosity measurements that similar orientation effects would occur in our cast films. In particular, we were interested in the perpendicular orientation favoring iridescence as a function of observation angle.

To that end, we used the StB toluene solution to develop a manual surface coating process to achieve iridescent films. We applied a blade casting method to StB solutions as shown in Figure 3b,c,e. Our metric for successful film formation was strong film iridescence, color uniformity throughout the film, and minimal film haziness. In our method, the StB solution was cast across a flat substrate (e.g., polymethylmethacrylate, PMMA). Figure 3b shows a schematic of the blading process of the polymer solution onto the substrate. On left and right sides of the substrates we applied multiple layers of tape to provide a rail for the casting blade that kept it at a constant gate height above the substrate surface during casting. To cast a film, the StB solution was first deposited in a thick line on the edge of the substrate between the tapes (Figure 3c), and then dragged with a blade across the substrate (Figure 3e). After solvent evaporation, an iridescent film formed (Figure 3f). To find the optimal conditions, we cast films at different gate heights (150–300 µm), different StB solution concentrations (5–11 wt%), and different casting speeds (0.5–3.0 cm s^{-1}), equivalent to shear rates of ≈20–100 s^{-1}. According to our metric best results were achieved for solution concentrations between 6.5 and 10 wt% and shear rates of 40–100 s^{-1}. We found that better film homogeneity was achieved, especially for larger film areas, by using higher casting speeds, lower concentrations, and larger gate heights. Smaller gate heights, making 1–5 µm thick films, led to fainter colors, possibly due to the resultant broadening of the FWHM of the Bragg reflection causing the "reflections" to be wavelength-independent.[55] Larger gate heights resulted in hazy films, which may have been related to the reorientation during drying of the toluene solution; if drying takes too much time, it is possible for significant reorientation to

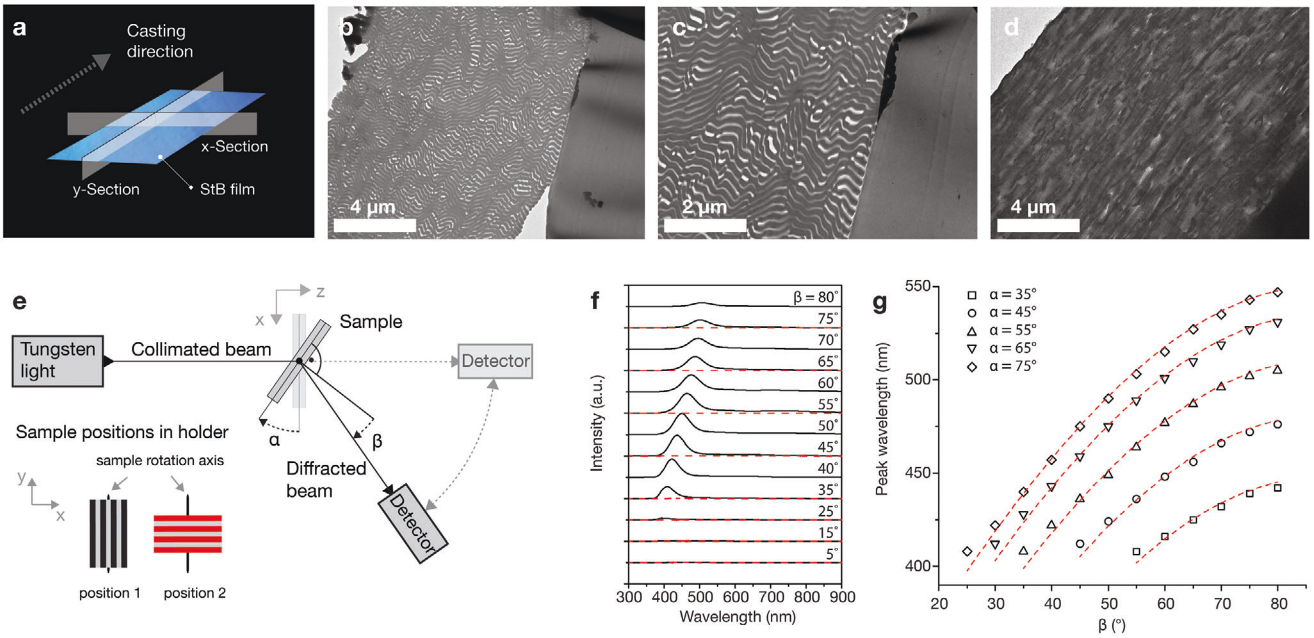

Figure 4. Structural and optical characterization of StB films. a) Definition of sample geometry. b–d) Transmission electron micrographs perpendicular (b, c; x-section in a), and parallel (d; y-section in a) to casting direction. e) Schematic of tunable spectrograph, showing different sample positions, vertical (1) and horizontal (2). f) Representative transmission diffraction measurements of StB-2 at $\alpha = 55^\circ$ in sample position 1 (black) and position 2 (red). g) Detection peak wavelengths against detector position, β, for different sample angles, α, for StB-2, fitted to the grating equation.

occur due to surface energy mismatch. For these ultra-large polymers, a reorientation into micellar structures could scatter light resulting in hazy films. Film quality was similar for different StB batches, however, as expected the color of films from StB batches of larger molar mass was red-shifted. The final dry StB films were ≈11 µm thick.

To probe the lamellar domain spacing, *d*, we characterized these films by USAXS (Figure 3d and Table 1). Figure S8 (Supporting Information) shows the domain spacing as determined by USAXS graphed against the molar mass as determined from Zimm plots of light scattering data (Figure S7, Supporting Information). The expected increase of *d*-spacing with molar mass was verified. Fitting the data points to a theoretical model with $d \propto M^{2/3}$,[56] with *M* being the weight average molar mass of the BCP, we find that the lower three molar mass samples (StB-1 to StB-3) follow the power law well with an exponent of 0.68 and a scale factor of 0.20. Deviation of sample StB-4 from expected behavior may be the result of the large amount of homopolymer in the sample and the associated asymmetry in composition (see Table 1; Figure S6, Supporting Information).

To further investigate the morphology of cast StB films we employed TEM. The top of **Figure 4** show cross-sectional TEM micrographs of a StB-2 film that was cast according to the conditions described above (for sample geometry, see Figure 4a). Figure 4b,c shows a cross-section at different magnifications taken perpendicular to the casting direction (x-section), while Figure 4d shows a cross-section taken parallel to the casting direction (y-section). While Figure 4b,c exhibits lamellae standing normal to the substrate, Figure 4d does not reveal any clear morphology. These results are consistent with the shear forces during the solution casting process introducing shear alignment into the film leading to lamellar sheets parallel to the casting direction and perpendicular to the substrate. This geometry agrees with distinctly different optical properties of films observed by eye in x- versus y-directions, i.e., perpendicular or parallel to the shear direction. Looking at StB films from different angles around the y-axis results in the observation of a color change ranging from dark blue to orange-red (less red for StB-1 and dark red for StB-4). In contrast, looking at films from different angles around the x-axis does not have noticeable color changing effects.

To quantitatively measure the angle-dependent optical properties of the StB films we used a tunable spectrometer setup as illustrated in Figure 4e. This instrument allowed us to measure the spectrum of light emitted from a white light source (tungsten light) and transmitted through the StB film as a function of sample orientation (incident angle α) and detection angle (β). Figure 4f shows a representative transmission measurement of a StB-2 film for incident light at $\alpha = 55^\circ$ and sample position 1 (sample rotation around *y*-axis/shearing direction). While keeping the light and sample steady the spectra at different detection angles, β, were measured in an arch around the sample center. A peak emerges ≈400 nm that shifts toward 500 nm for larger β. Repeating this experiment with a 90° rotated sample (sample position 2; sample rotation around x-axis/perpendicular to shearing direction), no signal is detected at respective angles, β (Figure 4f, red traces).

This can be explained by the orientation of the lamellar sheets resulting from the doctor blading method (Figure 3b). While the rotation around the sample *y*-axis, i.e., around the lamellar long axis, causes a change in the relative lamellar spacing and is detected by light of the excitation source, giving rise to angle dependent diffraction, the rotation around the sample *x*-axis (i.e., perpendicular to the lamellar long axis) does not influence the relative lamellar spacing. Consequently, no diffraction is observed for the given source/sample/detector geometry of this experiment. In Figure 4g the diffraction peak maxima are plotted against different detection angles, β, for different sample orientations ($\alpha = 35°$, $45°$, $55°$, $65°$, and $75°$). We found that the films behave according to a volume-phase grating with a grating periodicity of 282 nm. The grating periodicity was derived by fitting the data points to the transmission diffraction Equation (1)

$$\lambda_{max} = \Lambda_g \ (\sin(\alpha) + \sin(\beta)) \tag{1}$$

where Λ_g is the grating periodicity.[55] Remarkably, this result is the same as that from the USAXS measurement, which also measured 282 nm for the domain spacing. Table 1 summarizes results for all polymers StB-1 to StB-4 demonstrating that the optical measurements provided values well within 3% of the domain spacings, d, obtained from the USAXS measurements.

Of note, the TEM images in Figure 4b,c do show some orientational disorder of the lamellae. These imperfections in lamellar orientation can also explain the optical dispersion in the diffraction experiment shown in Figure 4f. The bandwidth, denoted by $\Delta\lambda/\lambda$, where λ denotes the peak wavelength and $\Delta\lambda$ denotes the FWHM of the peak, is on the order 0.1 in our experiment. For a perfect simple Bragg reflector, this value should be estimated as $(\Lambda/d)\cot(\alpha)$, where Λ is the periodicity (0.282 µm), d is the film thickness (≈10 µm), and α is the incident angle of the light, bringing the estimated value to ≈0.03. The discrepancy between the two values can be explained by the orientational disorder in the lamellae. This analysis suggests that an alternative casting method for such ultra-high molecular weight polymers may hold promise in creating a sharper Bragg reflector.

To complement the slender and smooth geometry of the needle tower, we aimed at homogenizing the color appearance of each window panel so as to smoothly blend one panel into the next, guiding the viewer's gaze along the structure, without breaking the flow by having different window panel color appearances. While it is easy to keep the appearance of multiple films the same on a small scale in the lab, i.e., by using the material from one synthesis batch, this is nontrivial for films on an architectural scale. Here, material demands easily exceed the capabilities of typical lab synthesis scales. For example, a typical synthesis yield of StB is about 35 to 40 g from a one-liter reactor with a success rate of 50%, mainly due to air or water contamination in the reactor (vide supra). However, we estimated a need of ≈500 g StB to fully cover the needle tower. We therefore scaled up the lab synthesis by a factor of two by using a custom made two-liter reactor equipped with a samarium cobalt stir bar (V&P Scientific) and a high-power stirring plate (KF-82, Yazawa Kagaku), which yielded 70–80 g material per successful batch. Further scale-up remained challenging both due to the lack of effective mixing during the polymerization as well as sufficient temperature-control of the reaction mixture. As a consequence, the window panels for the final tower had to be coated with BCP material from multiple batches, implying the use of varying molar mass samples, and consequently color variations as a result of poor control over absolute polymer molar mass. To address this issue, we investigated two strategies. Strategy one was to blend different StB batches with different molar mass together in solution and casting from such mixed batches (Figure S9a, Supporting Information). Strategy two was to adjust the color of each batch by swelling the domain spacing via addition of PS and PtBMA homopolymers (each ≈75 kg mol^{-1}) to the StB solutions (Figure S9b, Supporting Information). USAXS experiments on blended films from StB-2 and StB-3 (weight ratio 1:1) yielded a domain spacing lying between those of the original batches. Optical measurements supported this finding (**Table 2**; Figure S9c and S9, Supporting Information). The optical quality (i.e., transparency) of resulting films was not substantially compromised by the blending approach as suggested by similar full width at half maximum (FWHM) values of the optical transmission spectra for blended and original StB-2 and StB-3 derived films (Figures S9–S12, Supporting Information).

Table 2. USAXS and optical transmission diffraction measurement results for different batches of StB diblock copolymer films made by blade-casting for color tuning strategy one (batch blending) and two (StB, PS, and PtBMA homopolymer blending), respectively.

Sample	Mixing ratio StB-2:StB-3 or StB:PS:PtBMA [wt%]	*d* (*USAXS*) [nm]	Λ_g (*Diff.*) [nm]
StB-2	1:0/1:0:0	282	282 ± 2
StB-3	0:1	296	303 ± 1
StB-2/3	1:1	286	290 ± 10
StB-2a	8:1:1	N/A[a]	312 ± 1
StB-2b	4:1:1	353	333 ± 1
StB-2c	3:1:1	393	364 ± 1
StB-2d	1:1:1	N/A[a]	537 ± 5
StB (Tower blend)	All StB batches	N/A[b]	314 ± 1

[a] failed measurement; [b] not measured.

Strategy two also allowed us to tune film color by changing lamellar domain spacings of individual StB batches (Table 2; Figure S13, Supporting Information). However, the lamellar structure definition was substantially compromised with increasing amount of homopolymers added. This was apparent by eye in the form of film opacity as well as by a significant peak broadening both in USAXS as well as optical measurements (Figure S13, Supporting Information), leading to an increased discrepancy between d and Λ_g (within 8% of d). Therefore, we proceeded by using strategy one for the final installation.

Finally, we scaled the laboratory casting method up into a manual window panel fabrication method to produce 288 films, each 40 cm x 40 cm, for the final tower installation. The final casting solutions were composed of at least three to four synthesis batches to yield average film color appearances. For higher reproducibility of uniform films at this size, we found that faster casting speeds, ≈2.5–3.5 cm s^{-1}, coupled with decreased solution concentration of 6.5–7.5 wt% yielded best results. To counteract the increased shear speed, we increased the gate height to 250–300 µm. Due to the ultra-large molecular weight of our block copolymers being well past their entanglement molecular weight, it is likely the nanostructure of the StB film is a kinetically trapped state. A consequence of this, and the evaporation-induced self-assembly process, is that the lamellar spacing can depend on casting (solvent) conditions. Therefore, keeping

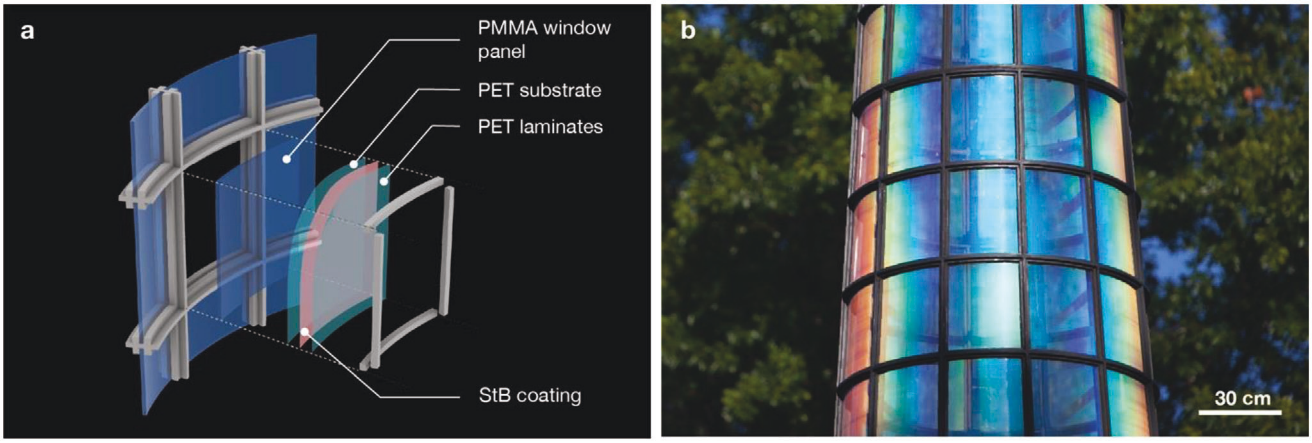

Figure 5. Window panel design. a) Schematic illustration of the window panel design. The PET-StB-PET sandwich is laminated to the concave side of the curved PMMA window panel. b) Final window panel of the installation.

solvent choice, blade casting, and drying conditions identical between films was critical for yielding consistent film quality. The use of blends between different ultra-high molecular weight polymer batches, strategy one from above, was another way to mitigate the challenge of potential film-to-film variations from the evaporation induced self assembly process, in addition to batch-to-batch variations. The blending method, combined with keeping the above key casting parameters consistent, worked to dependably reproduce the desired color and optical appearance of the film across each of the 288 40 cm × 40 cm panels.

The final goal was to achieve iridescent coatings for curved acrylic window panels. This complicated the process, since the manual film casting method described above was incompatible with curved/uneven substrates (any surface irregularity resulted in strongly visible smears in the StB films). To achieve coatings of curved surfaces using our casting method, we developed a casting-lamination technique. This technique consisted of two steps. In step one, the PET substrate was replaced by a thin, flexible PET lamination sheet with a thickness of ≈120 µm and a protected adhesive layer on its backside. This sheet was first adhered to a flat steel plate before solution casting (Figure S14a, Supporting Information). This was achieved by applying a thin layer of water-surfactant mixture (soap-water) between the PET sheet and the steel plate, leading to short range van-der-Waals interactions between the two and holding the PET sheet tightly to the surface of the steel plate. The resulting steel-PET substrate created a flat and stable substrate for solution casting. In step two, the PET sheet with the dry StB film coating (Figure S14b,c, Supporting Information) was removed from the steel plate and sandwiched under a second PET layer protecting against scratching and UV irradiation (**Figure** 5a).

This final PET-StB-PET sandwich was then cut into the desired size and laminated to the curved PMMA substrate to yield the final window panel (Figure 5b). The flexibility of the StB film laminated with the PET was more than sufficient to fit to the relatively low curvature of the acrylic windows without any noticeable distortion or delamination of the StB film. There were also no visible changes in optical quality of the films associated with their adjustment to the curved panels (see Movie S1, Supporting Information). In addition to the curved shape of the windows being a design goal for the installation, the PMMA and PET further served to protect the mechanical and optical durability of the StB films. PMMA is well known to be UV-opaque, and the sandwiching of the structurally colored films by PET was an additional UV shield. Furthermore, the PET lamination and robust PMMA windows act as a physical shield to the outside world. The effectiveness of this design in the optical and mechanical longevity of the StB films is demonstrated by the installation still being on display with no noticeable optical degradation after a decade.

In an effort to investigate the potential of our casting method to produce iridescent coatings on alternative substrates, we applied it to paper. Unlike the previous PMMA and PET substrates, paper is composed of pressed cellulose fibers producing a porous surface. Despite this difference, we were able to apply the same approach as described above. We found that best results were achieved using gate heights for film casting of 300–350 µm. To our surprise, an iridescent film formed that adhered well to the substrate surface and remained flexible without delaminating from the paper. **Figure** 6a–c illustrates the properties of this coated paper using the example of a periodic Miura-ori pattern and an iridescent origami crane. SEM images in Figure 6d reveal that the StB film is able to wrap around the paper fibers. A cross-sectional TEM image (Figure 6e) reveals a lamellar morphology with lamellar sheets standing normal to the substrate surface, similar to what we saw in Figure 4b,c for the dense, solid polymer substrates.

In order to increase material longevity and robustness, processing and coating of iridescent organic–inorganic hybrid films was explored as an alternative to all-organic materials. To this end, amphiphilic BCPs, SA-1 (1257 kg mol^{-1}) and SA-2 (1304 kg mol^{-1}) were synthesized (for synthesis scheme, see Figure S15, Supporting Information, and for polymer characterization results, please see **Table** 3; Figures S16 and S17, Supporting Information). Unlike, StB, SA contains a hydrophilic block, PDMAEMA, that can be selectively swelled with inorganic precursors in solution.[57] The main precursor chosen was Durazane 1800, a polysilazane that is commercially available and used for producing chemical-and-environmental-resistant coatings. A 1.37:0.13 mixture by mass of Durazane 1800 and GLYMO,

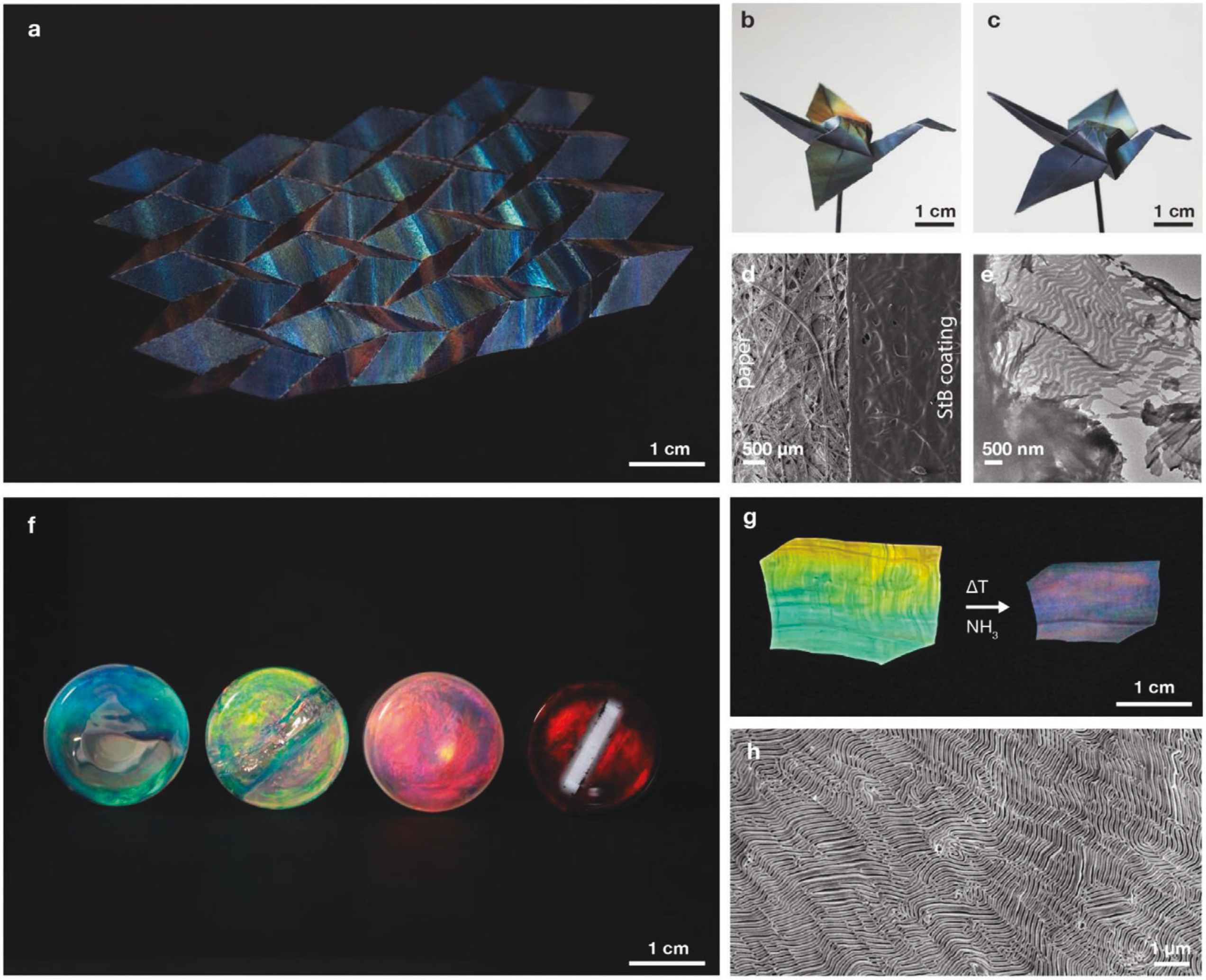

Figure 6. Applications of iridescent block copolymer coatings and materials. a) Photograph of black paper with iridescent coating. b,c) Photographs of an origami paper crane showing a comparison of the left wing at different viewing angles. The papers were coated with StB applying a modified solution casting method. d) Top-down SEM image of StB coated paper. e) Cross-sectional TEM image of StB coated paper perpendicular to casting direction showing the lamellar BCP morphology. f) Photograph of SA:Durazane 1800 bulk preceramic hybrid gels in the bottom of scintillation vials. The blue sample (far left) is from a 1:1.37 SA-2:Durazane 1800 mixture (by weight) and after stirring for ≈2 h. The green sample (second from left) is from a 1:1.37:0.13 SA-2:Durazane 1800:GLYMO mixture (by weight), resulting in an organic: inorganic weight ratio of 1:1.5 and more green-shifted coloration. The pink sample (second from right) is from a 1:1 mixture of SA-1 and SA-2 and a 1:1.37 polymer:Durazane 1800 mixture (by weight) after 6 h of stirring. The dark red sample (far right) was realized by adding 0.1 wt% carbon black to the same initial solvent mixture as for the pink sample and stirred for >12 h. g) Photograph of an iridescent hybrid film from a 1:1.37 SA-2:Durazane 1800 mixture (by weight, left), and that same film subsequently converted at 1000 °C in ammonia to an iridescent silicon oxynitride ceramic (right). h) Cross-section SEM image of the ceramicized iridescent film in (g).

an organically modified precursor for silica, was further explored in some samples to alter composition. These components were mixed in a ternary solvent mixture of toluene, allyl acetate, and benzyl acetate at 10–12.5 wt% concentrations to generate a one-pot polymer hybrid dope. Similar to the StB films, mixing SA polymers could be used to tune hybrid dope color, in this case mixing SA-1 and SA-2 in a 1:1 mass ratio red-shifted the color of the dope, e.g., relative to SA-1 derived materials.

Table 3. Polymer characterization results for SA. Weight average molar mass, determined by Zimm plots, and PS block volume percent, determined by proton NMR.

Sample	M_W [kg mol^{-1}]	f_{PS} [vol%]
SA-1	1257 ± 144	0.80
SA-2	1304 ± 48	0.65

The dope was doctor bladed onto glass substrates with a similar technique to casting StB. The films were left to dry for >12 h due to the high boiling points of the solvents used. Once fully dried, films were crosslinked for 12 h at 130 °C. The resultant hybrid films were iridescent, well-adhered to the glass substrate, and rigid. These films were made at a higher gate height, and therefore greater thickness, than the StB films to make them more robust against subsequent thermal treatments.

Due to the increased thickness of these films, they were less transparent and homogenously colored at a single viewing angle than the StB films; rather, these films were more translucent and showed intense and variable coloration. For the hybrid film shown in Figure 6g (left), the colors range from blue-green to orange when viewed at an angle. This inhomogeneity of the color and clarity of the hybrid films is likely due to longer evaporation times, relative to the StB films, caused by larger film thickness and the choice of solvents for compatibility of the hybrid system resulting in reorientation of the sheared lamellar domains to less organized structures (see Figure 6h for SEM images of these domains after ceramization). Since composite bulk films of co-assembled BCP and Durazane 1800 have previously been used to generate mesostructured ceramic films[58] the hybrid films were next tested to see if a porous iridescent ceramic could be obtained. To that end, hybrids were thermally treated to 1000 °C under ammonia atmosphere, resulting in a ceramic that demonstrated structural color (Figure 6g, right). As Figure 6g suggests, thermally treating such hybrid films to the corresponding ceramics resulted in physical shrinking, while the general shape of the bulk film was maintained. Furthermore, the color of the ceramics were blueshifted as compared to the hybrid films, showing predominantly a violet-blue structural color. This is consistent with shrinking of the block copolymer directed nanodomains via loss of the organic structure directing agent during thermal treatment. Figure 6h shows a cross-sectional SEM of the porous ceramic, which features lamellar bands of ceramic and void space. From these SEM images, the ceramic portion of the nanostructure has domain sizes >100 nm. Together with the relatively large refractive index difference of air and such silicon nitride-type ceramics, this is consistent with leading to the observed structural color.

4. Conclusion

We introduced a novel BCP-based art material developed through an art-science collaboration between the Wiesner Lab at Cornell University and the artist Kimsooja. This material was featured prominently in the installation ‘A Needle Woman: Galaxy Was a Memory, Earth is a Souvenir’. We successfully developed a material synthesis and processing workflow for biomimetic pathways to create iridescent thin film coatings that are tunable in color, largely compatible with traditional film and substrate coating processes, and durable enough to endure the use in outdoor settings. To transition from lab scale BCP research to a uniformly iridescent BCP façade coating for an architecture installation required overcoming obstacles on three separate scales. First, the lamellar BCP domain spacing needed to be large enough (>100 nm) to interact with visible light for obtaining the desired optical film properties, i.e., iridescent colors spanning the entire visible spectrum while maintaining optical transparency of the window panels. This was achieved by scaling the BCP chains to exceptionally large molar mass (>1000 kDa) and casting thin films onto PMMA or PET substrates. Second, the BCP batch synthesis needed to be scaled up to synthesize sufficient amounts of material (i.e., 0.5 kg) to cover large areas with the BCP film. Despite increased synthesis amounts in our labs a single batch synthesis was not sufficient to produce enough material to cover the entire structure. To guarantee a mostly homogenous color appearance, we blended separate BCP batches of StB without substantially sacrificing optical film quality. Finally, an appropriate StB coating process needed to be developed to cover large areas (≈46 m^2) with a thin StB film, which additionally needed to be applicable to curved substrate surfaces. This was achieved by a manual casting-lamination process, which took advantage of the shear-rate-dependent alignment of the lamellar morphology to produce coloration that changes with viewing angles. Additionally, we discovered that the same StB casting method could be adapted for use on porous substrates, such as paper. We demonstrated its application in producing iridescent origami paper, suitable not only for origami art but also offering potential applications in fashion design and other creative fields. To demonstrate the ability of an amphiphilic BCP to co-assemble with an additive to make an innately structurally colored hybrid material that could be thermally processed into a structurally colored functional material, a one-pot synthesis of an inorganic porous ceramic bulk film with self-assembled structural color was designed and executed. An amphiphilic BCP, SA, was synthesized and co-assembled with a ceramic precursor, Durazane 1800; the resultant hybrid iridescent film was converted into a ceramic via thermal processing at 1000 °C under ammonia and retained its structural color. We thus achieved robust, iridescent films from both a purely organic system and from an inorganic and porous functional material.

In reflection, this project serves as an example how the collaboration between artists and scientists is the continuation of a human history of discovery and the constant quest for novel expression and meaning. Materials have always shaped artistic practices, frequently acting as a foundational element in both the creation of art and its perception. Consequently, we argue that comprehending the constraints imposed by art materials is crucial for gaining insight into aesthetic preoccupations and the historical significance of art.

Furthermore, the division of disciplines, i.e., the arts and the sciences, places materials in a cultural context, e.g. “scientific materials” (or state-of-the-art materials) present in laboratories and used for research and “art materials” found in art studios and used for the creation of art. When artists engage with scientific materials, these materials undergo a profound recontextualization, transitioning from their original, often purely analytical or functional purposes, to embody new meanings and evoke emotional or intellectual responses within an aesthetic framework. This recontextualization is not merely a shift in application, but a transformation in how these materials are perceived and understood by audiences. Scientific materials, once embedded within the domain of art, are imbued with layers of interpretation, challenging viewers to see beyond their original contexts. Through this creative alchemy, art-science collaborations not only broaden the scope of what materials can convey but also bridge the gap between the empirical world of science and the interpretive, subjective experience of art. This fusion not only makes science more accessible to the public but also invites a reflective examination on the nature of materials science and society at large.

Supporting Information

Supporting Information is available from the Wiley Online Library or from the author.

Acknowledgements

F.F.E.K., H.S. and W.R.T.T. contributed equally to this work. This paper was funded through the National Science Foundation (DMR-2307013). The authors gratefully acknowledge Kimsooja and Kimsooja Studio, Jaeho Chong, and Stephanie Owens (Cornell Council for the Arts) for the opportunity to participate in this project. F.F.E.K., H.S., and U.B.W. gratefully acknowledge Troy Batugal, Camila S. Brey Gil, Zhe Chen, Andrew Moorman, and Max Vanatta for the help in the panel production. F.F.E.K. thanks Dr. Warren Zipfel for helpful discussions and experimental assistance as well as access to optical parts. F.F.E.K. thanks Dr. Frank Wise and Dr. Eduardo Mendes for inspiring and helpful discussions and Dr. Rahul Mangal for experimental assistance with rheological measurements. This work made use of the Cornell Center for Materials Research shared facilities which were supported through the NSF MRSEC program (DMR-1719875) at Cornell. W.R.T.T. gratefully acknowledges the Department of Energy for financial support through Grant No. DE-SC0010560. Furthermore, this research used resources of the Advanced Photon Source, a U.S. Department of Energy (DOE) Office of Science user facility operated for the DOE Office of Science by Argonne National Laboratory under Contract No. DE-AC02-06CH11357. W.R.T.T. thanks the Cornell University Insect Collection for access to their specimens.

Conflict of Interest

The authors declare no conflict of interest.

Data Availability Statement

The data that support the findings of this study are available from the corresponding author upon reasonable request.

Keywords

architectural nanomaterials, art-science collaboration, biomimicry, block copolymer self-assembly, structural color

Received: September 15, 2024
Revised: November 7, 2024
Published online: December 5, 2024

---

[1] M. Aubert, R. Lebe, A. A. Oktaviana, M. Tang, B. Burhan, A. J. Hamrullah, B. H. Abdullah, J. Zhao, I. M. Geria, P. H. Sulistyarto, R. Sardi, A. Brumm, *Nature.* **2019**, *576*, 442.
[2] I. Domingo, A. Chieli, *Archaeol. Anthropol. Sci.* **2021**, *13*, 196.
[3] D. J. Barber, I. C. Freestone, *Archaeometry.* **1990**, *32*, 33.
[4] R. Zong, X. Lu, W. Li, C. Xu, *Archeometry.* **2024**, 1, https://doi.org/10.1111/arcm.12969.
[5] P. C. Gutierrez, T. Pradell, J. Molera, A. D. Smith, A. Climent-Font, M. S. Tite, *J. Am. Ceram. Soc.* **2010**, *93*, 2320.
[6] A. Verney-Carron, L. Sessegolo, A. Chabas, T. Lombardo, S. Rossano, A. Perez, V. Valbi, C. Boutillez, C. Muller, C. Vaulot, B. Trichereau, C. Loisel, *npj Mater. Degrad.* **2023**, *7*, 49.
[7] B. H. Berrie, L. C. Matthew, *Scientific Examination of Art: Modern Techniques in Conservation and Analysis*, The National Academies Press, Washington, DC **2005**.
[8] P. Dear, *Isis.* **2005**, *96*, 390.
[9] V. Gewin, *Nature.* **2021**, *590*, 515.
[10] E. Kac, in *Telepresence, Biotelematics, and Transgenic Art*, Kibla, Maribor, Slovenia **2000**.
[11] A. K. Yetisen, A. F. Coskun, G. England, S. Cho, H. Butt, J. Hurwitz, M. Kolle, A. Khademhosseini, A. J. Hart, A. Folch, S. H. Yun, *Adv. Mater.* **2015**, *28*, 1724.
[12] P. Ball, *Nat. Mater.* **2016**, *15*, 500.
[13] M. Michael, *Sci., Technol., Human Values.* **2018**, *43*, 1098.
[14] K. Nassau, in *The Physics and Chemistry of Color: The Fifteen Causes of Color*, 2nd ed., Wiley-VCH, Hobokin, NJ **2001**.
[15] Z. Xuan, J. Li, Q. Liu, F. Yi, S. Wang, W. Lu, *Innovation.* **2021**, *2*, 100081.
[16] C. Finet, *Humanit. Soc. Sci. Commun.* **2023**, *10*, 348.
[17] J. H. Hah, S. Mayya, M. Hata, Y. Jang, H. Kim, M. Ryoo, S. Woo, H. Cho, J. Moon, *J. Vac. Sci. Technol. B.* **2006**, *24*, 2209.
[18] M. Braglia, I. V. Ferrari, T. Djenizian, S. Kaciulis, P. Soltani, M. L. Di Vona, P. Knauth, *ACS Appl. Mater. Interfaces.* **2017**, *9*, 22902.
[19] T. Thuen-Albrecht, J. Schotter, G. A. Kästle, N. Emley, T. Shibauchi, L. Krusin-Elbaum, K. Guarini, C. T. Black, M. T. Tuominen, T. P. Russell, *Science.* **2000**, *290*, 2126.
[20] R. Ryoo, S. H. Joo, S. Jun, *J. Phys. Chem. B.* **1999**, *103*, 7743.
[21] M. Templin, A. Franck, A. Du Chesne, H. Leist, Y. Zhang, R. Ulrich, V. Schädler, U. Wiesner, *Science.* **1997**, *278*, 1795.
[22] R. Li, S. Zhang, R. Zhang, *Chem. Methods.* **2023**, *3*, 202200081.
[23] H. Li, P. Wu, G. Zhao, J. Guo, C. Wang, *J. Colloid Interface Sci.* **2021**, *584*, 145.
[24] H. S. Lee, T. S. Shim, H. Hwang, S. Yang, S. Kim, *Chem. Mater.* **2013**, *25*, 2684.
[25] S. D. Rezaei, Z. Dong, J. Y. E. Chan, J. Trisno, R. J. H. Ng, Q. Ruan, C. Qiu, N. A. Mortensen, J. K. W. Yang, *ACS Photonics.* **2021**, *8*, 18.
[26] Y. Zhou, C. Jia, K. Lu, C. Wang, L. Ma, L. Liu, *Sol. Energ. Mater. Sol Cells.* **2023**, *259*, 112459.
[27] K. Li, C. Li, H. Li, M. Li, Y. Song, *iScience.* **2021**, *24*, 102121.
[28] P. Cencillo-Abad, D. Franklin, P. Mastranzo-Ortega, J. Sanchez-Mondragon, D. Chanda, *Sci. Adv.* **2023**, *9*, eadf7207.
[29] H. Kim, J. Ge, J. Kim, S. Choi, H. Lee, H. Lee, W. Park, Y. Yin, S. Kwon, *Nat. Photon.* **2009**, *3*, 534.
[30] B. M. Boyle, T. A. French, R. M. Pearson, B. G. McCarthy, G. M. Miyake, *ACS Nano.* **2017**, *11*, 3052.
[31] Y. Liu, H. Wang, J. Ho, R. C. Ng, R. J. H. Ng, V. H. Hall-Chen, E. H. H. Koay, Z. Dong, H. Liu, C. Qiu, J. R. Greer, J. K. W. Yang, *Nat. Commun.* **2019**, *10*, 4340.
[32] S. Yu, Q. Zhang, Y. Wang, Y. Lv, R. Ma, *Nano Lett.* **2022**, *22*, 4925.
[33] J. H. Kim, H. M. Jin, G. G. Yang, K. H. Han, T. Yun, J. Y. Shin, S. Jeong, S. O. Kim, *Adv. Funct. Mater.* **2020**, *30*, 1902049.
[34] M. Stefik, S. Guldin, S. Vignolini, U. Wiesner, U. Steiner, *Chem. Soc. Rev.* **2015**, *44*, 5076.
[35] M. Poutanen, G. Guidetti, T. I. Gröschel, O. V. Borisov, S. Vignolini, O. Ikkala, A. H. Gröschel, *ACS Nano.* **2018**, *12*, 3149.
[36] E. Kim, S. Y. Kim, G. Jo, S. Kim, M. J. Park, *ACS Appl. Mater. Interfaces.* **2012**, *4*, 5179.
[37] L. Han, D. Xu, Y. Liu, T. Ohsuna, Y. Yao, C. Jiang, Y. Mai, Y. Cao, Y. Duan, S. Che, *Chem. Mater.* **2014**, *26*, 7020.
[38] A. M. Urbas, M. Maldovan, P. DeRege, E. L. Thomas, *Adv. Mater.* **2002**, *14*, 1850.
[39] Y. La, J. Song, M. G. Jeong, A. Cho, S. Jin, E. Lee, K. T. Kim, *Nat. Commun.* **2018**, *9*, 5327.
[40] D. Ndaya, R. Bosire, R. M. Kasi, *ACS Appl. Polym. Mater.* **2020**, *2*, 5511.
[41] Z. Wang, C. L. C. Chan, R. M. Parker, S. Vignolini, *Angew. Chem., Int. Ed.* **2022**, *61*, 202117275.
[42] Y. Kang, J. J. Walish, T. Gorishnyy, E. L. Thomas, *Nat. Mater.* **2007**, *6*, 957.
[43] A. C. Edrington, A. M. Urbas, P. DeRege, C. X. Chen, T. M. Swager, N. Hadjichristidis, M. Xenidou, L. J. Fetters, J. D. Joannopoulos, Y. Fink, E. L. Thomas, *Adv. Mater.* **2001**, *13*, 421.
[44] D. Song, G. Jacucci, F. Dundar, A. Naik, H. Fei, S. Vignolini, J. J. Watkins, *Macromolecules* **2018**, *51*, 2395.

[45] *Tell us your Lab to Fabulous story, Nat. Rev. Electr. Eng.* **2024**, *1*, 67.
[46] J. Chong, *Space.* **2015**, *566*, 116.
[47] Y. S. Park, https://ysp.org.uk/about-ysp, (accessed: August 2024).
[48] F. Schacher, T. Rudolph, F. Wieberger, M. Ulbricht, A. H. E. Müller, *ACS Appl. Mater. Interfaces.* **2009**, *1*, 1492.
[49] B. H. Zimm, *J. Chem. Phys.* **1948**, *16*, 1093.
[50] J. Ilavsky, P. R. Jemian, A. J. Allen, F. Zhang, L. E. Levine, G. G. Long, *J. Appl. Crystallogr.* **2009**, *42*, 469.
[51] J. Ilavsky, F. Zhang, A. J. Allen, L. E. Levine, P. R. Jemian, G. G. Long, *Metall. Mater. Trans. A.* **2013**, *44*, 68.
[52] I. W. Hamley, in *The Physics of Block Copolymers*, Oxford Univ. Press, Oxford, England **1998**.
[53] G. G. du Sart, R. Rachmawati, V. Voet, G. Alberda van Ekenstein, E. Polushkin, G. ten Brinke, K. Loos, *Macromolecules.* **2008**, *41*, 6393.
[54] U. Wiesner, *Macromol. Chem. Phys.* **1997**, *198*, 3319.
[55] I. K. Baldry, J. Bland-Hawthorn, J. G. Robertson, *PASP.* **2004**, *116*, 403.
[56] Y. Matsushita, K. Mori, R. Saguchi, Y. Nakao, I. Noda, M. Nagasawa, *Macromolecules.* **1990**, *23*, 4313.
[57] T. N. Hoheisel, K. Hur, U. B. Wiesner, *Prog. Polym. Sci.* **2015**, *40*, 3.
[58] E. M. Susca, P. A. Beaucage, M. A. Hanson, U. Werner-Zwanziger, J. W. Zwanziger, L. A. Estroff, U. Wiesner, *Chem. Mater.* **2016**, *28*, 2131.